

1st Year CSI Report: Part 1

Near-fault Ground Motion Prediction, Site Effects and Wave Propagation at Regional Scale for a Shallow Earthquake in Southeast France

PhD student: Hongyi SU^{1,2}

Thesis supervisors: Sébastien HOK¹, Mathieu CAUSSE², Céline GELIS¹,
Cécile CORNOU²

CSI committee: Bertrand DELOUIS³, Céline BEAUVAL²

¹Bureau d’Evaluation des Risques Sismiques pour la Sécurité des Installations (BERSSIN), IRSN,
Fontenay-aux-Roses, France

²Institut des Sciences de la Terre (ISTerre), UGA, Grenoble, France

³Laboratoire Géoazur, Université de la côte d’Azur, France

Key Points:

- The 2019 Mw4.9 Le Teil earthquake was a shallow, moderate-magnitude event that ruptured at the surface, causing significant damage near the epicenter. Despite its moderate magnitude, this type of earthquake poses a substantial threat to sensitive infrastructures like nuclear power plants (NPPs). To understand the variability and intensity of ground motions in such scenarios, it is essential to perform scenario-based earthquake modeling since near-fault ground motion records for this and similar earthquakes globally are missing.
- We estimate dynamic parameters from final fault slip distribution within the slip-weakening friction framework using the latest kinematic model proposed by Bertrand Delouis (updated in August 2023).
- We use an open-source code SeisSol (<https://seissol.org/>) to perform 3D dynamic rupture modeling and generate synthetic ground motion on the free surface for the 2019 Mw 4.9 Le Teil earthquake, using previously estimated dynamic parameters.

Abstract

Kinematic source parameters such as rupture size, duration, velocity, initiation location, and slip rate can be routinely explored through existing inversion codes after an earthquake, facilitated by readily available high-quality strong motion, teleseismic waveform, as well as geodetic measurements. In contrast, physics-based dynamic parameters are not constrained by observational dataset, they represent the physical processes occurring on the fault, for example, dynamic traction evolution and fault weakening process. In dynamic rupture models, the final slip is evaluated from rupture evolution governed by fault constitutive relations called friction laws, and slip-weakening friction is perhaps the easiest one among them.

However, physics-based dynamic rupture models often struggle to match with observational records unless supplemented with data-driven information. In this study, we introduce a novel method to infer dynamic parameters from final slip distribution. We utilize the slip-weakening friction law, where the fracture energy is determined by the critical slip weakening distance D_c , static and dynamic friction coefficients, μ_s and μ_d . We apply our approach to a shallow, moderate-sized earthquake in southeastern France, the final slip comes from a recent kinematic rupture model.

We present two dynamic rupture models derived from the same kinematic model but with different levels of smoothing. The low-smoothed kinematic model exhibits higher slip than the strongly smoothed one. In our method, we create 3D spherical patches at the point sources of the kinematic model, where the size of each patch and the critical slip distance d_c within it are determined by the final slip. As a result, the connectivity of these spherical patches varies between the two models, leading to different rupture histories and causing variability in the computed synthetic waveforms.

Given the absence of high-quality near-source observations for this event, our physics-based modeling may have an answer to a crucial question: what is the intensity of ground motion experienced in the epicentral area during the earthquake? The synthetic accelerograms computed from our preferred dynamic rupture model indicates the maximum vertical acceleration locally exceeding gravity, with rapid decay over distance.

1 Introduction

The 2019 Mw 4.9 Le Teil earthquake was a shallow moderate event, which ruptured to the surface and caused significant epicentral damage. It shows that moderate magnitude earthquake can represent a significant threat to infrastructures located close to a fault and its ground motions (GM) have to be properly predicted. However, records of near-fault ground motion (NFGM) for this and similar events worldwide are limited. To understand the variability and intensity of expected NFGMs, synthetic NFGM including source, propagation, and site effects is required. Le teil Earthquake is a good study case for this purpose, since we can simulate ground motions on a virtual sensor array and explore uncertainties and impacts associated with the different physical parameters relevant for rupture, wave propagation and site effects modeling.

An accurate fault rupture model is crucial for NFGM modeling, especially when the fault rupture is shallow and reaches the surface. As a matter of fact, it is expected that NFGM levels and variations are closely linked to rupture details, seismic radiation being controlled by slip velocity and rupture velocity variations. For the source modelling, it is possible to use either kinematic and/or dynamic descriptions. We will combine both approaches, since they have complementary advantages and limitations. Kinematic modeling strengths are: calibration with data through inversion for the low frequency part, fast computation allowing sensitivity and variability studies and linear broadband waveform generation from power law description of slip characteristics. On the other hand, kinematic modeling has limitations such as: details of rupture process mostly controlled by man-controlled assumptions having an impact on final GM variability, no physical control on the source parameters implying possible un-physical models and GM. The dynamic modeling advantages are: incorporation of local physical constraints such as fault geometry, rock mechanics, stress field, free surface, etc. Their limitations are: frictional parameters not easy to calibrate, computationally demanding. In summary, kinematic models allow to explore a wider parameter space to quantify impacts of uncertainties on parameters controlling the NFGM in our specific configuration (e.g. slip distribution, slip velocities, rupture velocities). However, we will start using the rupture dynamics to restrain the combination of parameters to those which are physically consistent with our scenario and specific case (fault geometry, stress field, physics of rupture, wave propagation along and around the fault). Geological structure also influences NFGM. We will thus also study the impact of the soil structure according to the local velocity model. Figure 1 illustrates a simplified flowchart of the modeling process. The initial part of the work will be to define a reference dynamic model, based on a set up of friction parameters (inferred consistently with available reference source model), initial stress (including geology and velocity structure) and other observations.

The results of our simulations will be compared with in-situ observations of objects displaced by the earthquake, which have made it possible to obtain quantitative measurements of the ground acceleration near the fault (Causse et al., 2021). This work is part of a process of validation of near-field GM models (e.g. Valentova et al. 2021) for hazard calculations.

Once our reference physical (dynamic) model is calibrated, we will allow variations of some parameters such as shallow layer properties, medium mechanics (off fault plasticity), small scale features (smoothing). This step will allow to quantify the impact of the source parameters on the ground motions, and tackle the main goal of this thesis: generate broadband near fault ground motion based on rupture physics and local site conditions (using kinematic techniques for instance).

At the end of the first year, we have been working essentially on the reference dynamic model. We perform dynamic rupture modeling with the code *SeisSol*.

SeisSol is a 3D dynamic rupture solver where seismic wave emission is coupled with dynamic fault slip. The emitted seismic waves propagate through 3D elastic media and are reflected by the free surface. These waves are recorded by virtual receivers on the free surface. The two main outputs from a dynamic rupture model are coupled stress change / fault slip and the seismic wave field. To utilize the available kinematic model, we introduce a novel method to estimate dynamic parameters from the final slip distribution within the slip-weakening friction framework.

Our preliminary results suggest the variability and intensity of synthetic NFGM depend on the input slip distribution. Generated NFGM locally exceeds gravity with a rapid decay over distance from the epicenter, strong directivity was observed in the synthetic NFGMs.

In the end, we analyze and compare the similarities and differences between our 3D physics-based dynamic rupture model and the kinematic slip model proposed by B. Delouis (2023), as well as previous Le Teil source characteristics by Delouis et al. (2021), Cornou et al. (2021), Causse et al. (2021), Ritz et al. (2020), Mordret et al. (2020), and De Novellis et al. (2020) De Novellis et al. (2021), alongside the 3D physics-based model by Smerzini (2022) and the 3D dynamic rupture models by Aochi & Tsuda (2023) and Rihab Sassi (PhD Thesis).

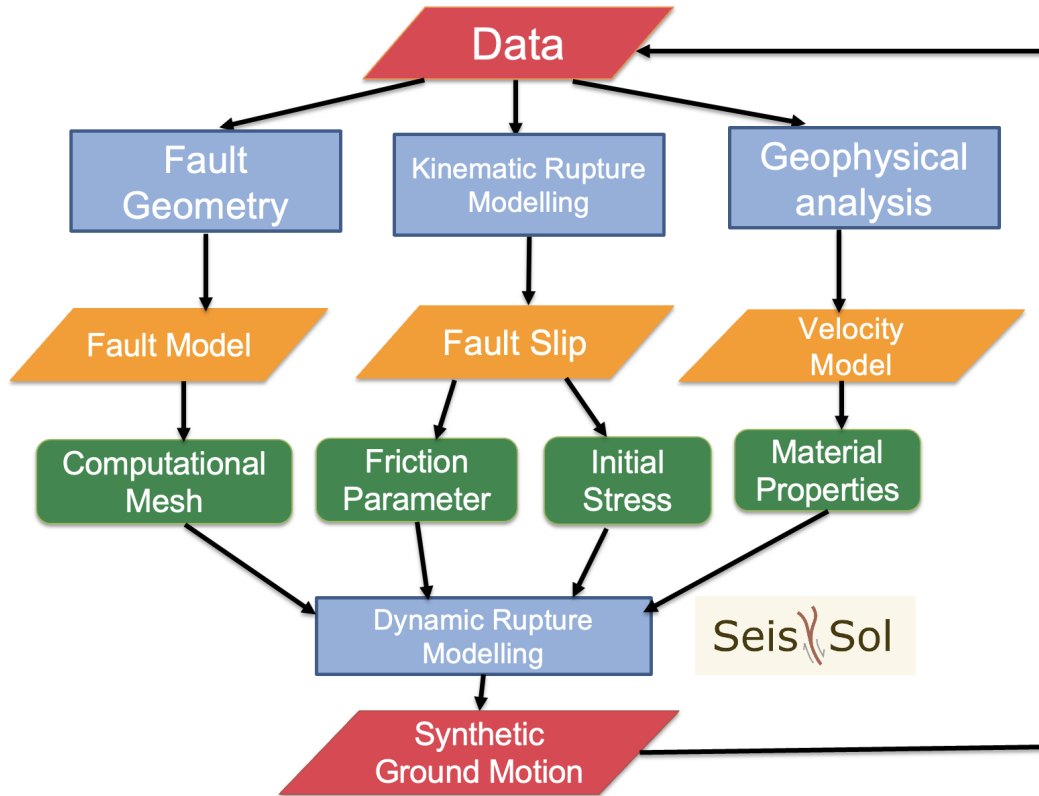


Figure 1: Conceptional workflow for kinematic model informed dynamic rupture modelling using the simulation code SeisSol

2 Model setup

Figure 2 shows a topographic map of the studied area. The black box outlines the boundary of the computational mesh, and the yellow star marks the epicenter. The blue line indicates the fault trace, while the green triangles represent near-fault virtual receivers. Red triangles are observational stations, with two located inside the mesh boundary; the distance of station ADHE to the epicenter is noted as 18.20 km. Additionally, two NPPs are marked on the map with blue and green diamonds.

Cornou et al. (2021) provide the first response to the event by various French institutions together, including the development of seismometers around the epicentral area after the mainshock and a preliminary static slip model of the rupture. Ritz et al. (2020) provided comprehensive observational evidence about the event characteristics, including geological, seismological, geodetic, and field observations. Delouis et al. (2021) use different seismological techniques to relocate the mainshock. All these three authors agree that the Le Teil earthquake has a reverse faulting focal mechanism and is localized on the SE dipping La Rouvière fault (LRF) (Cornou et al., 2021; Ritz et al., 2020). Geologic evidence shows the LRF fault resides in a region in which faults result from different tectonic episodes, and the ancient Oligocene LRF normal fault was reactivated as reverse faulting during the 2019 Le Teil earthquake (Cornou et al., 2021; Ritz et al., 2020). In situ stress measurements suggest the current regional stress field is NW-SE compressional, with a maximum NW-SE strain rate of $0.7e-9yr^{-1}$ (Masson et al., 2019). Ritz et al. (2020) found the LRF fault also matches with InSAR discontinuity with an exception on the NE segment. Notable exceptions led the authors to speculate an unmapped fault that extends to the SE of the NE part of the LRF to which the deformation is transferred. They also estimated the total surface deformation produced by the earthquake and observed the vertical fault offset could reach 15 cm. The deformation appears to be larger and more localized in the SW part of the LRF (ref. Fig 4 (Ritz et al., 2020)) and with wider accommodation zone in the north (400 - 800 m ref. (Ritz et al., 2020)) compared to the south (50 - 400 m, ref. Ritz et al. (2020)). Moreover, Ritz et al. (2020) determined the moment magnitude using the following rupture parameters listed in *Table 1.1* with the equation $Mw = 2/3 \log(M_0) - 6.7$, where $M_0 = \mu LWD$. For comparison, we also listed the same parameters used in Cornou et al. (2021). Note that for fault slip D , Ritz et al. (2020) assume a constant dip angle of 45° , while Cornou et al. (2021) use 58° . Both studies generally agree with each other, but Ritz et al. (2020) provide more details and uncertainty analysis to justify their parameter choices.

Table 1: Reported rupture parameters for the Le Teil earthquake

Parameter	Ritz et al 2020		Cornou et al 2021	
	value	unit	value	unit
μ	$2e10 - 2.5e10$	Pa	$3e10$	Pa
L	4600 - 5200	m	5000	m
W	1400 - 2800	m	1740	m
D	0.10	m	0.4	m
Vr	-	-	1.8	km/s
M_0	-	-	$2.7e16$	Nm
M_w	4.7 - 5.0	-	4.9	-

The source parameters reported in the two studies mentioned above, plus Delouis et al., 2021 are listed in *Table 1.2*. Ritz et al.(2020) found their best solution, strike/dip/rake = 50/45/89, based on an FMNEAR waveform inversion (Delouis, 2014), where the strike

can vary between 45° to 65° and the dip can vary between 45° to 50° . Delouis et al. (2021) use the same method as Ritz et al. (2020) and found the dip angle is not well constrained by the FMNEAR waveform inversion due to very shallow depth of the earthquake. they proposed a dual velocity model that incorporated two distinct 1D velocity models for the NW and SE areas instead of a 1D depth-dependent velocity model as used in the inversions by Ritz et al. (2020). The best solution for strike/dip/rake corresponds to 48/45/88, which is not too different from the values reported by Ritz et al. (2020), but the dual model is better consistent with geology, i.e. it addresses particularly high Vp/Vs ratio (1.8 - 1.9, ref. (Delouis et al., 2021)) in the SE domain, and it significantly improves waveform fitting (RMS decrease from 0.59 to 0.416, ref. (Delouis et al., 2021)).

The epicentral location showed in Cornou et al. (2020) includes rapid revisions of Geoazur/OCA, OSUG/SISMALP, ReNass, CEA-LDG, and CSEM, but all of them located the mainshock on the wrong side of the fault (Delouis et al., 2021). This motivated Delouis et al. (2021) to carried out a detailed investigation on epicentral relocation with growing available observational data, they especially benefited from the recorded seismic data for an ML 2.8 aftershock 12 days after the mainshock, and relocated the mainshock more accurately based on a master event technique (Delouis et al., 2021). They exclusively used P and S arrival times without prior constraints on depth range, and reported the average solution of epicentral latitude, epicentral longitude, and hypocentral depth for the mainshock as 44.5188N, 4.6694E, and 1.3km (ref. (Delouis et al., 2021)). A quarry blast has also been carried out to reinforce the solution(ref. (Delouis et al., 2021)). Ritz et al. (2020) use similar epicentral locations as Delouis et al.(2021) for their inversion.

Table 2: Reported source parameters for the Le Teil earthquake

Parameter	Ritz et al. 2020		Cornou et al. 2021		Delouis et al. 2021	
	value	unit	value	unit	value	unit
dip	45 - 50	$^\circ$	58	$^\circ$	45 - 60	$^\circ$
strike	45 - 65	$^\circ$	50	$^\circ$	40 - 45	$^\circ$
rake	89	$^\circ$	89	$^\circ$	88	$^\circ$
lat	44.518	N	44.521	N	44.5188	N
lon	4.671	E	4.669	E	4.6694	E
depth	1-3	km	1-3	km	1-2	km

To conclude, all three studies confirmed the 2019 Mw4.9 Le Teil earthquake was a superficial event that occurred on an SE dipping reserve fault with hypocentral depth being shallower than 1.5 km (Ritz et al., 2020; Cornou et al., 2021; Delouis et al., 2021). They all agree on rupture area, epicentral location, and bilateral rupture style. We will model this event using law of physics based on those knowledge, i.e. the rupture and source parameters listed in *Table 1* and *Table 2*.

2.1 Computational Mesh

The computational mesh for our current model is simplified. We do not consider topography and basin, Our current computational mesh consists of around 2 million unstructured tetrahedron elements, representing a volume of $10 \text{ km} \times 10 \text{ km} \times 8.5 \text{ km}$. The resolution of elements is 25 meters on the fault, coarsening away with a gradient rate of 0.5.

Figure 3 shows a clipped view of the mesh, with the dark hues indicating the fault plane. The inclined flat surface represents the La Rouvière Fault (LRF), and the fault

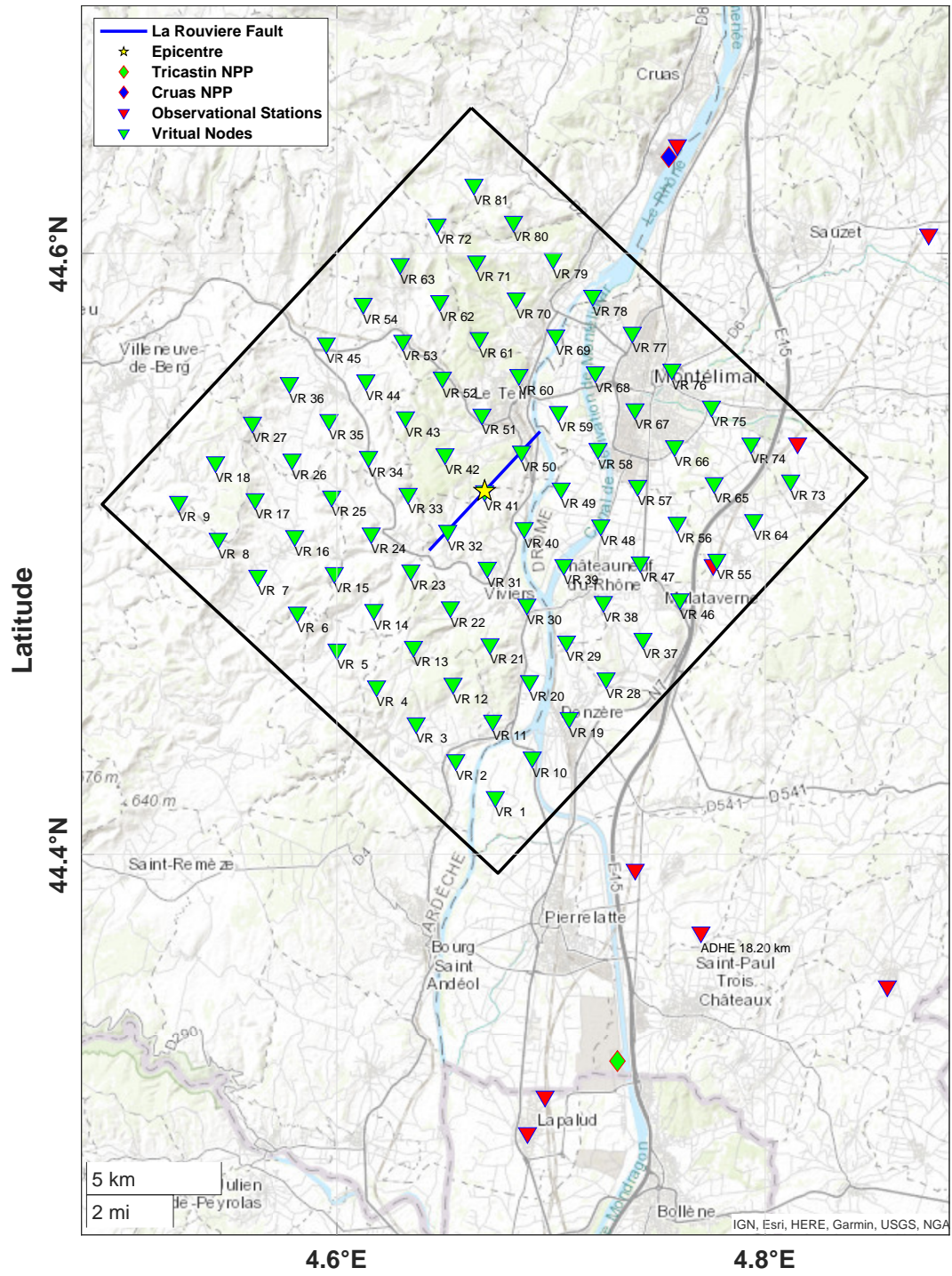


Figure 2: Map of the studied area. The black box shows the boundary of the computational mesh.

geometry parameters used for reconstruction are summarized in Table 3, same as the kinematic model by Bertrand Delouis. Dip angle indicated in the Table 3 is also confirmed by a recent aftershock study (Godano, Larroque et al., personal communication).

Note that for simplification, all computations are done with strike=90, then we rotate the coordinates of virtual stations after computation when comparing the synthetic ground motion with observations, which is equivalent to change the fault strike in the model but easier to achieve numerically (requiring a smaller model).

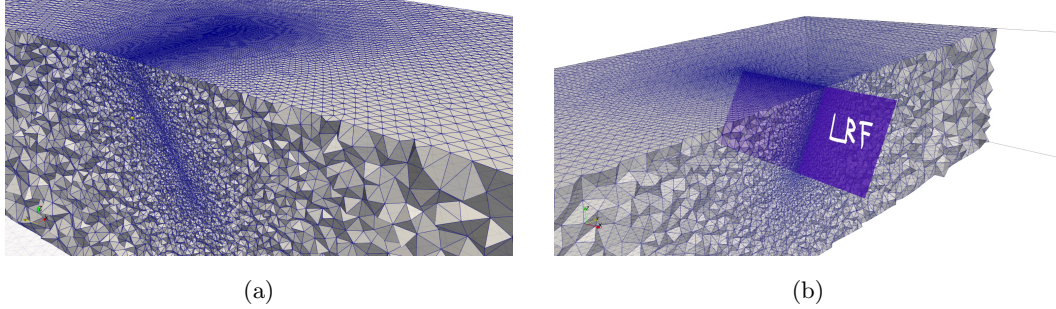


Figure 3: Reconstruction of the La Rouvière Fault (Fault) with unstructured tetrahedron mesh elements for the Le Teil area.

Table 3: Fault Geometric Parameters

Width [km]	Length [km]	Dip	Strike	Hypocentre Coordinate (m)
2.5	6	57	47	(0,0,-1000)

2.2 Fault Slip

From a list of static/kinematic slip models for the Le Teil earthquake (Delouis et al. (2021), Cornou et al. (2021), Ritz et al. (2020), De Novellis et al. (2020), Mordret et al. (2020)), we selected the most recent kinematic model by Bertrand Delouis (updated August 2023), which was jointly inverted using seismological and geodetic datasets. The models with strong and low smoothing levels are shown in Figure 4

We create spherical patches based on the multipoint kinematic slip model, using two criteria: first, each point source (subfault) must be shallower than 1.5 km; second, the cumulative slip magnitude at the point must exceed 8 cm, as specified in the source code available here. Figure 5 illustrates the resulting spherical patches from the strong- and low-smoothed kinematic slip models. The spherical patch is three-dimensional, with its centre located on the fault plane, making the on-fault spherical patch the largest circle of the ball. Each point source's XYZ coordinates serve as the center of the ball, and the patch's radius is scaled according to the magnitude of the accumulated slip at each point source. We introduce a scale factor λ to control the size of the patches from a trial-and-error approach, for example, 0.02 in this model. This scaling is necessary to ensure the patches connect with one another without excessive overlap. If overlap occurs, the parameters within the overlapped areas will be overwritten by the last assigned value.

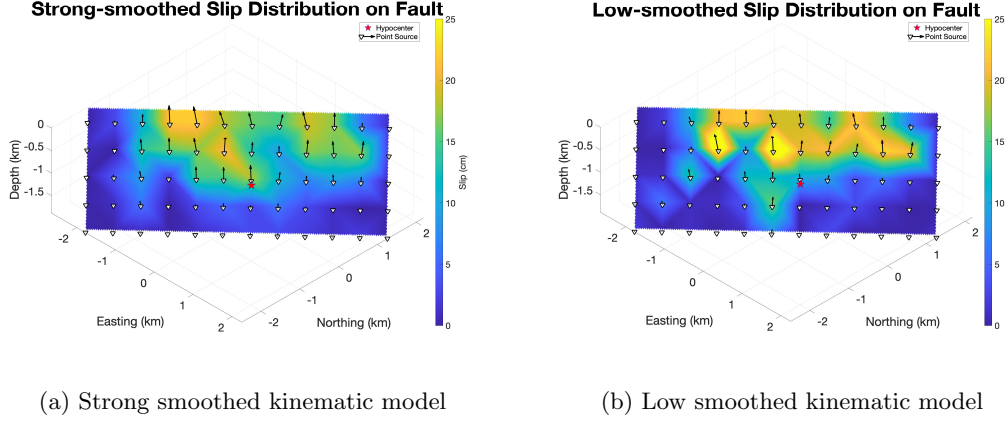


Figure 4: Comparison of the kinematic models between strong- and low-level of smoothing. Each kinematic model comprises 60 point sources. We display the rake angle at each source as a vector, with the length scaled according to the slip magnitude, illustrating the direction of the slip. The red star denotes the hypocenter.

In Figure 6, we experiment with different λ , using slightly larger and lower values. Figure 6a shows a scenario where all patches are isolated, while Figure 6b depicts a case where the patches excessively overlap each other.

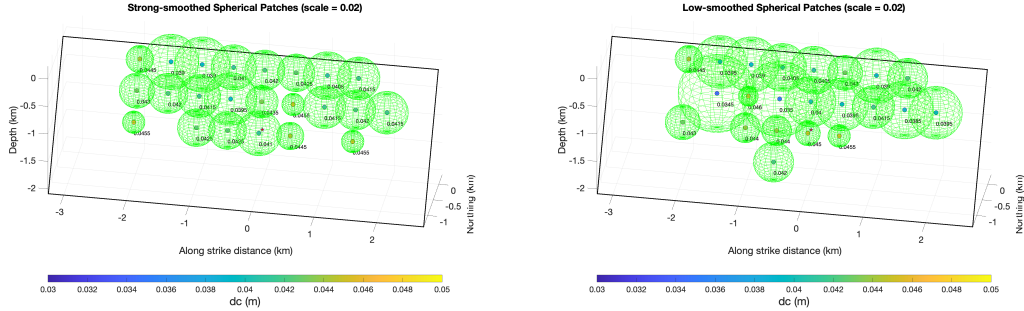
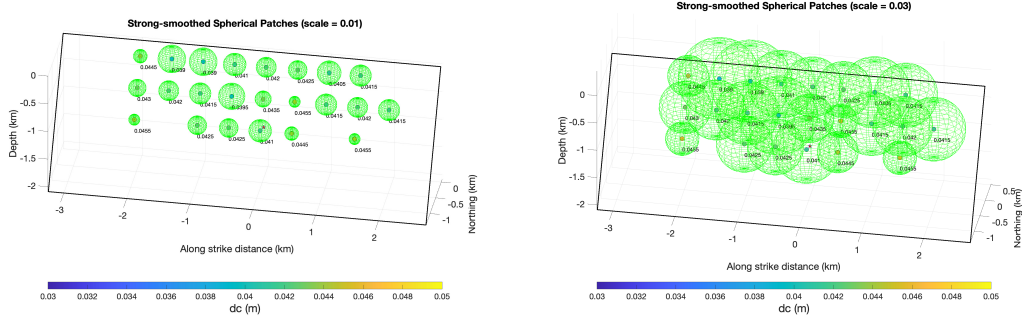


Figure 5: Comparison of the spherical patches from two kinematic models with strong- and low-level of smoothing. We use a scale factor λ to control the size of the spherical patches.

After creating the spherical patches, we put specific frictional parameters inside each one. We use the linear slip-weakening (LSW) friction law to control how the fault ruptures (Ida (1972); Andrews (1976)). Table 4 lists the dynamic rupture parameters. μ_s and μ_d mean the static and dynamic friction coefficients. D_c is the critical slip-weakening distance, where shear stress drops from its peak to residual stress (Palmer & Rice (1973);



(a) Strong-smoothed spherical patches model,
scale parameter = 0.01

(b) Strong-smoothed spherical patches model,
scale parameter = 0.03

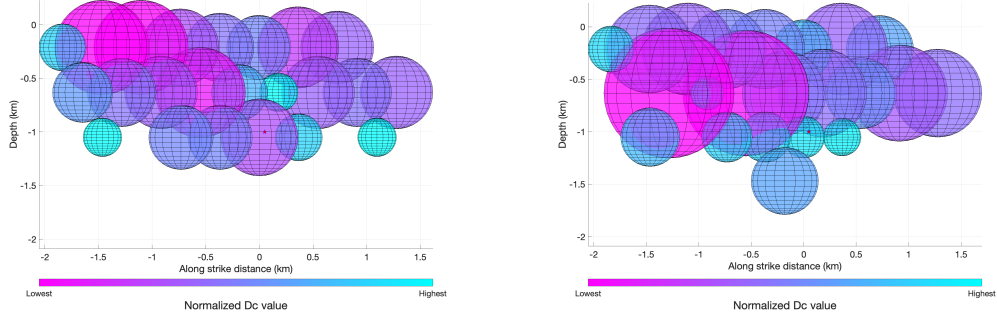
Figure 6: Comparison of spherical patches with different scale

Bizzarri & Cocco (2003)). c is cohesion. We set μ_s and μ_d at constant values of 0.6 and 0.2 respectively everywhere. D_c scales with slip, and we choose the value for c carefully for three different situations. We set it to 2 MPa for shallower layers to reduce the effect of the free surface, 0 MPa inside the patches to promote fault slip, and 10 MPa outside the patches to prevent fault slip.

Table 4: Frictional Parameters in the Model (Used D_c scaling)

	Inside Patch	Outside Patch
μ_s	0.6	0.6
μ_d	0.2	0.2
D_c (m)	$0.05 * (1 - \text{slip (in meters)})$	0.05
c (MPa)	0 / 2 (in shallow layers)	10

In Figure 7, the distribution of normalized D_c values across the fault plane is presented for both setups. In the setup on the left, a high D_c patch is observed, surrounded by regions of low D_c . This high D_c patch, due to its high fracture energy, will stop dynamic rupture from passing through it and force the rupture propagation take a detour.



(a) Normalized D_c distribution in spherical patches created from strong smoothed slip model on the fault plane

(b) Normalized D_c distribution in spherical patches created from low smoothed slip model on the fault plane

Figure 7: Comparison of normalized D_c distribution

The selected values for static and dynamic friction coefficients (μ_s and μ_d) are commonly used in dynamic rupture modeling. Byerlee's law (Byerlee (1978)) suggests that the strength of rock increases uniformly with depth, irrespective of its composition. Within the spherical patches, D_c is reduced proportionally to the total fault slip distance and capped at 0.05 m. However, accurately determining D_c is challenging, leading most dynamic rupture simulations using the linear slip-weakening (LSW) friction law to adopt a constant D_c value across the entire fault plane. Nevertheless, Ohnaka (2013) demonstrated that D_c correlates with spatial irregularities on the fault, indicating its likely variability across the fault Venegas-Aravena et al. (2022). The relationship between D_c and final slip was explored in Tinti et al. (2009), where statistical findings suggested D_c can be computed as 40% of the total slip distance. In this model, D_c increases proportionally to the total fault slip distance while maintaining a constant ratio D_c/D_{tot} . So dynamic frictional parameters with values detailed in Table 5 might be more convincing.

Table 5: Frictional Parameters in the Model (Tinti's D_c scaling)

	Inside Patch	Outside Patch
μ_s	0.6	0.6
μ_d	0.2	0.2
D_c (m)	$0.4 * (\text{slip})$	0.05
c (MPa)	0 / 2 (in shallow layers)	10

Simple dynamic rupture models often use homogenous frictional parameters across the whole fault plane when not incorporated with data-informed information. For example, the dynamic rupture modeling performed by Aochi & Tsuda (2023) also utilizes slip-weakening friction. In their model, the parameters are set as follows: $\mu_s = 0.6$, $\mu_d = 0.33$, $c = 5\text{MPa}$, and $D_c = 0.05\text{m}$ throughout the fault plane.

2.3 Velocity Model and Site Effects

Figure 8 and Table 6 illustrate and list the layered velocity model utilized in the dynamic modeling, adapted from Causse et al. (2021). Figure (a) displays a smoothed layered velocity model, processed with a Gaussian filter, in a 3D mesh, including fault slip of a model realization.

We did not take site effect into account in our current setups. The smallest shear velocity in our current model is around 1200 m/s with small modifications due to the applied Gaussian smoothing filter. A more detailed velocity model focusing on shallow depths would be necessary to explore site amplification.

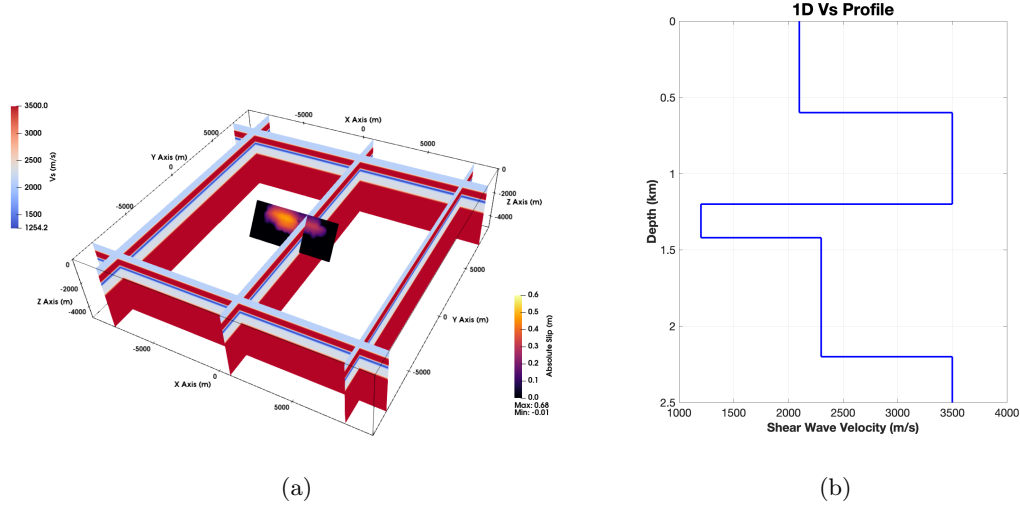


Figure 8: (a) Display of smoothed layered velocity model (Gaussian filter) in 3D mesh, plotted with fault slip of a model realization (b) 1D layered velocity model from Causse et al., 2021

Table 6: Velocity Model of Causse et al. (2021)

Depth [km]	0.0	0.63	1.2	1.42	2.03	2.19	5.96
Density [kg/m^3]	2407	2688	2165	2465	2470	2667	2685
V_s [m/s]	2047	3645	1200	2291	2314	3457	3616

2.4 Weak Nucleation

We adopted the weak nucleation method as outlined in Tinti et al. (2021). This method is preferred over the overstressing method, which often leads to artificially large fault slip in the hypocentral area and generates unrealistic strong pulses in synthetic seismograms, as observed in Palgunadi et al. (2020). The adopted approach gradually reduces the yield strength within an elliptical area centered at the hypocenter. Over time, this area expands at a decreasing speed, as described in Harris et al. (2018). This strategy ensures a smooth transition to fully spontaneous dynamic rupture propagation. In our models,

the forced nucleation phase lasts for less than 1.67 seconds with minimal moment release, utilizing a nucleation initial forcing speed of 300 m/s and a nucleation radius of 0.5 km.

2.5 Strain-constrained S-parameter

The S parameter is the ratio between stress excess (peak stress - initial stress) and dynamic stress drop (initial stress - residual stress). Before performing dynamic rupture simulations, we can predict rupture growth based on the model's S profiles.

S is defined as (Andrews (1976)Das & Aki (1977)),

$$S = \frac{\tau_p - \tau_0}{\tau_0 - \tau_r} \quad (1)$$

$$\begin{cases} S < 0 & \text{unfavorable} \\ 0 \leq S \leq 1 & \text{favorable} \\ S >> 1 & \text{unfavorable} \end{cases} \quad (2)$$

Strain-consistency constraint means we do not allow the strain of the upper layers to exceed the lower layers (Aochi & Tsuda, 2023Aochi & Tsuda (2023)). The constrained strain is deviatoric, it is calculated as deviatoric stress ($\frac{1}{2} \cdot (\sigma_1 - \sigma_3)$) divided by the shear modulus of each layer.

We have reproduced the model of Aochi and Tsuda (2023). The input parameters are summarized in the Table 7, the 1D layered velocity model is from Causse et al., (2021) Causse et al. (2021)

Input parameters for the model of Aochi and Tsuda (2023)							
$dip = 50$	$s2ratio = 0.5$	$R = 1$	$\alpha = 0$	$\mu_d = 0.33$	$\mu_s = 0.6$	cohesion = 5 MPa	
depth [km]	0.0	0.63	1.2	1.42	2.03	2.19	5.96
ρ [kg/m ³]	2407	2688	2165	2465	2470	2667	2685
V_s [m/s]	2047	3645	1200	2291	2314	3457	3616

Table 7

Figure 9 shows the comparison of maximum and minimum principal stresses and normal stress before and after the strain consistency constraint.

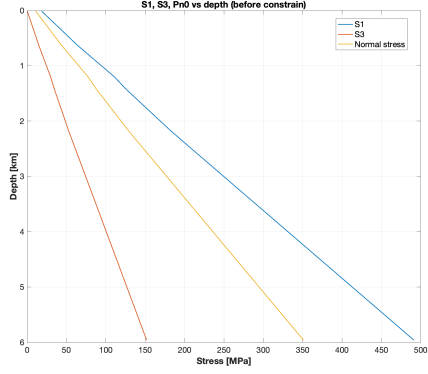
Figure 10 shows the comparison in peak, initial, and residual stresses before and after the strain consistency constraint. We can see at some layer boundaries, initial stress is lower than redial stress.

Figure 11 shows S parameter becomes negative at some depths after applying the strain consistency condition.

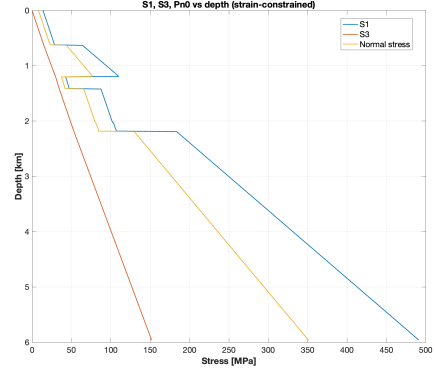
Figure 12 compares the strain before and after the constraint and display the 1D layered rheological model.

2.6 Initial Stress

The initial stress is based on Anderson's theory of faulting and the Mohr–Coulomb theory of fault failure Ulrich, Gabriel, et al. (2019). The stress was mapped using an easi

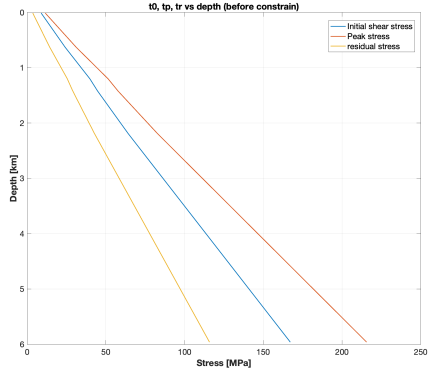


(a)

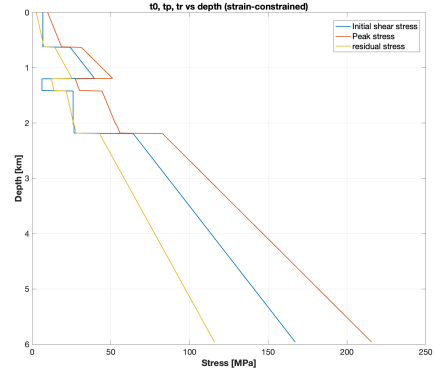


(b)

Figure 9: S1, S3 and normal stress as a function of depth. (a): before strain-constrained condition (b): after strain-constrained condition



(a)



(b)

Figure 10: t0, tp and tr as a function of depth. (a): before strain-constrained condition (b): after strain-constrained condition

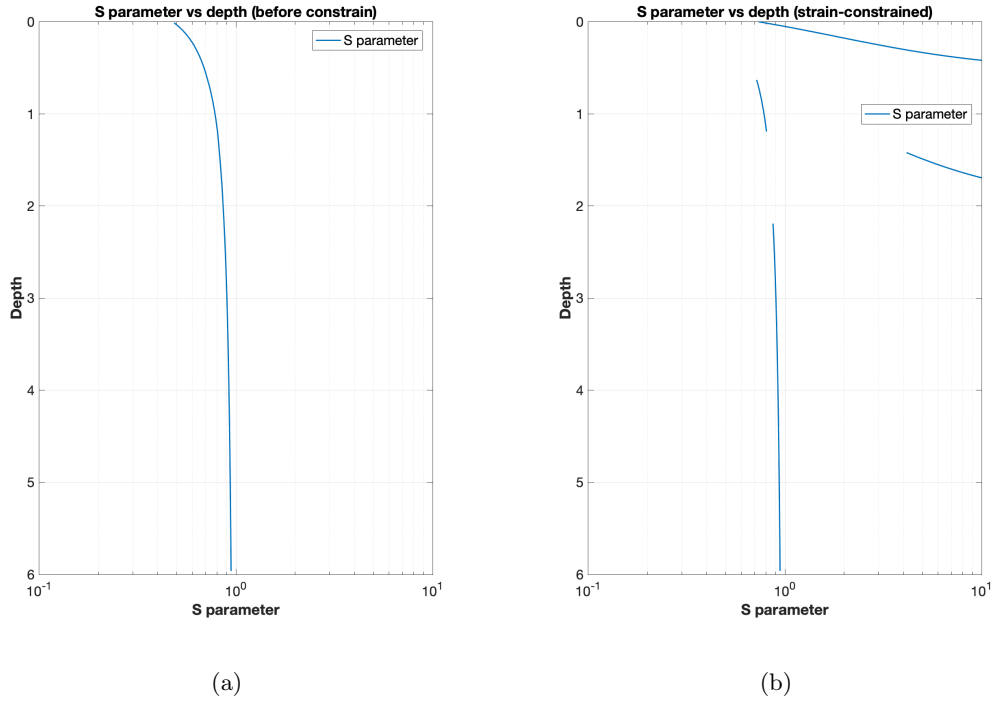


Figure 11: S parameter before and after applied strain constrained condition

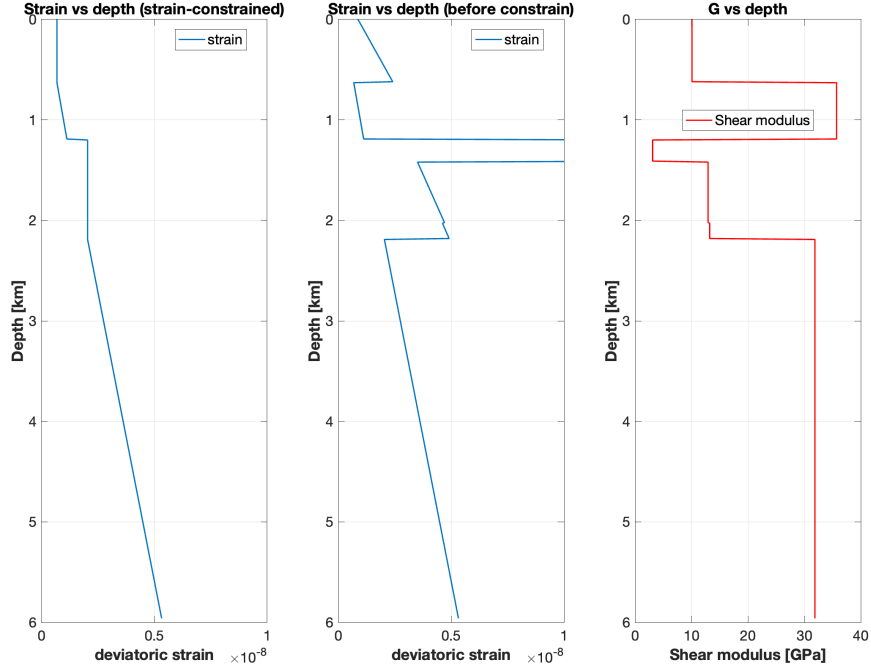


Figure 12: From left to right: strain vs depth (after strain constrained condition), strain vs depth (before strain constrained condition), shear modulus vs depth

function, AndersonStress (Carsten Uphoff, 2018). The input parameters are summarized in Table 8.

Table 8: Stress Parameters in the easi function

μ_s	0.6
μ_d	0.2
SH_{max}	0
S_v	3
<i>cohesion</i>	0
<i>s2ratio</i>	0.4
S	0.2 (0-1km) / negative (1km)
sig_{zz}	$\rho(z)*g*z$

Similar to frictional parameters in the LSW friction law, here μ_s and μ_d are the static and dynamic friction coefficients, respectively. SH_{max} is the azimuth of the maximum horizontal shear stress, which is a challenging parameter to estimate Zoback (1992). For simplicity, we set $SH_{max} = 0$, means that the maximum horizontal shear stress is perpendicular to the fault, resulting in nearly zero along-strike shear stress and maximum along-dip shear stress, as seen in Figure 19. $S_v = 3$ indicates that the vertical principal stress is σ_3 , which agrees with Anderson’s theory of faulting for a reverse faulting mechanism. We set cohesion to 0, assuming that the surrounding rock is not cohesive. The *s2ratio* is the ratio between σ_1 , σ_2 , and σ_3 , also known as the stress shape ratio, which characterizes the stress regime, 0.4 indicates transpression Ulrich, Vater, et al. (2019). The S parameter represents the ratio between initial shear stress, peak shear stress, and residual shear stress. When S is positive and small, conditions facilitate spontaneous dynamic rupture. Conversely, when S is large or negative, it indicates that conditions are not conducive to dynamic rupture Aochi & Tsuda (2023). For simplicity, we set the S parameter to 0.2 for all depths above 1 km and negative for all depths below 1 km. Finally, σ_{zz} defines the lithostatic loading.

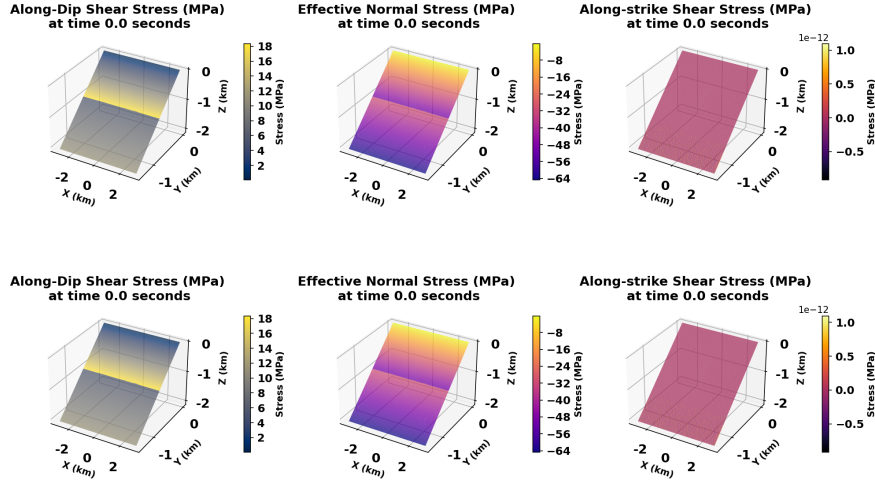


Figure 13: From left to right: initial shear stress in the dip direction, initial effective normal stress, and initial shear stress in the strike direction on the fault plane. The top panel shows the strong-smoothed model and the bottom panel shows the low-smoothed model.

3 Dynamic rupture Results

3.1 Source Time Function

Figure 14 (a) shows the source time function of the dynamic models. Here, we name the low-smoothed kinematic model as kinematic model 1, and the strong-smoothed kinematic model as kinematic model 2. The corresponding dynamic models are called dynamic model 1 and 2. The source time function represents the energy release measured as seismic moment over time, with the time integral of seismic moment yielding moment magnitudes of 4.92 and 5.05 for dynamic models 1 and 2, respectively, which align with the target magnitude.

From this curve, we can estimate the rupture duration to be around 2 seconds, consistent with kinematic modeling from Causse et al. (2021). In the low-smoothed model, the two peaks in the source time function correspond to two asperities, with each peak representing the rupture of one asperity. In contrast, the strong-smoothed model exhibits a single large peak in the source time function, indicating that the two asperities on both sides rupture simultaneously, contributing to the high peak in the source time function curve.

Figure 14 (b) presents the Fourier spectrum of the source time function, revealing that the dynamic and kinematic models exhibit similar decaying slopes. The source time function of dynamic model 2 closely matches that of kinematic model 2, because the two asperities in dynamic model 2 release energy sequentially rather than simultaneously.

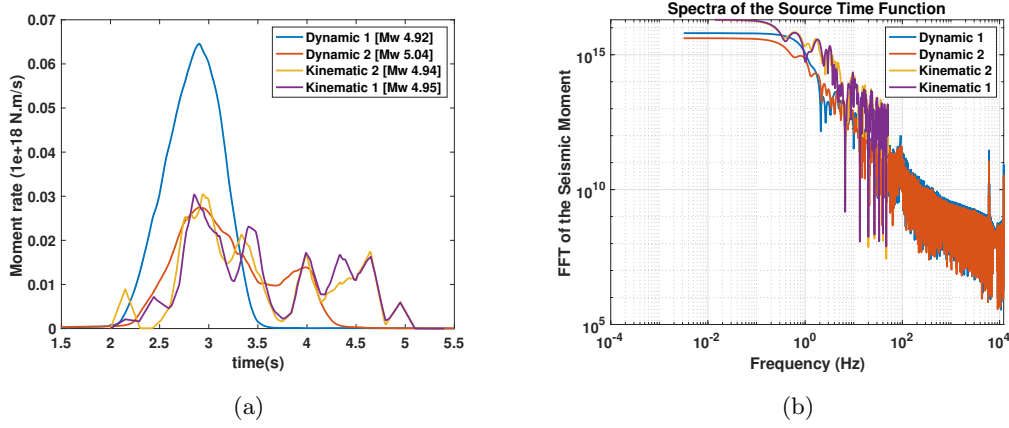
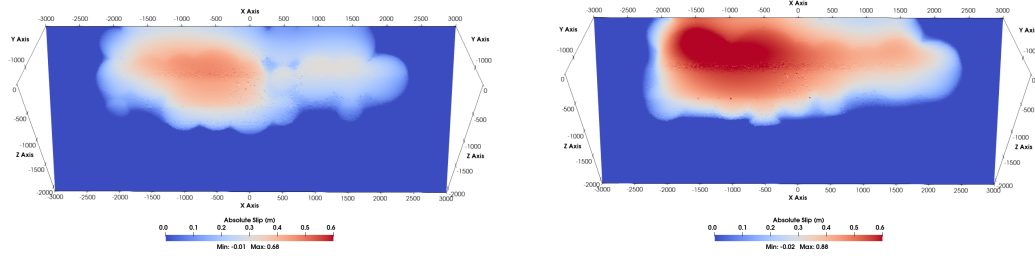


Figure 14: (a) Source time function of low- and strong-smoothed kinematic models and resulting dynamic models, they are noted as Kinematic model 1 and 2, dynamic model 1 and 2 (b) Spectrum of the source time function

3.2 Final Slip

The model derived from the strong-smoothed kinematic model displays two distinct asperities, whereas the other model only has one large asperity and demonstrates larger final slip values compared to the former.

Both models exhibit a similar final slip pattern to the starting kinematic model. Unfortunately, we lacked quantifiable metrics for direct comparison.



(a) Final absolute slip on the fault plane for the dynamic rupture model from the strong-smoothed kinematic model.

(b) Final absolute slip on the fault plane for the dynamic rupture model from the low-smoothed kinematic model.

Figure 15: Comparison of the final absolute slip between the dynamic rupture model derived from the strong- and the low-smoothed kinematic model

3.3 Slip Rate History on Fault

We compare the along-dip slip rate history for both models. Figure 16 displays the dynamic rupture model derived from the strong-smoothed kinematic model, while Figure

17 shows the model derived from the low-smoothed kinematic model. The snapshots are from 2.2 seconds to 4.4 seconds with a time step of 0.2 seconds.

In the strong-smoothed model, the rupture progresses from the west side of the fault to the east side after nucleation, whereas in the low-smoothed model, rupture propagates simultaneously in both directions. This difference is due to the connectivity of the spherical patches and explains the observed source time function.

Both models exhibit pulse-like behavior, with the slip rate abruptly dropping to 0 after the rupture Gabriel et al. (2013). We did not observe the generation of supershear waves in the simulation. Instead, conical wave fronts are visible, traveling faster than the shear wave speed in that layer.

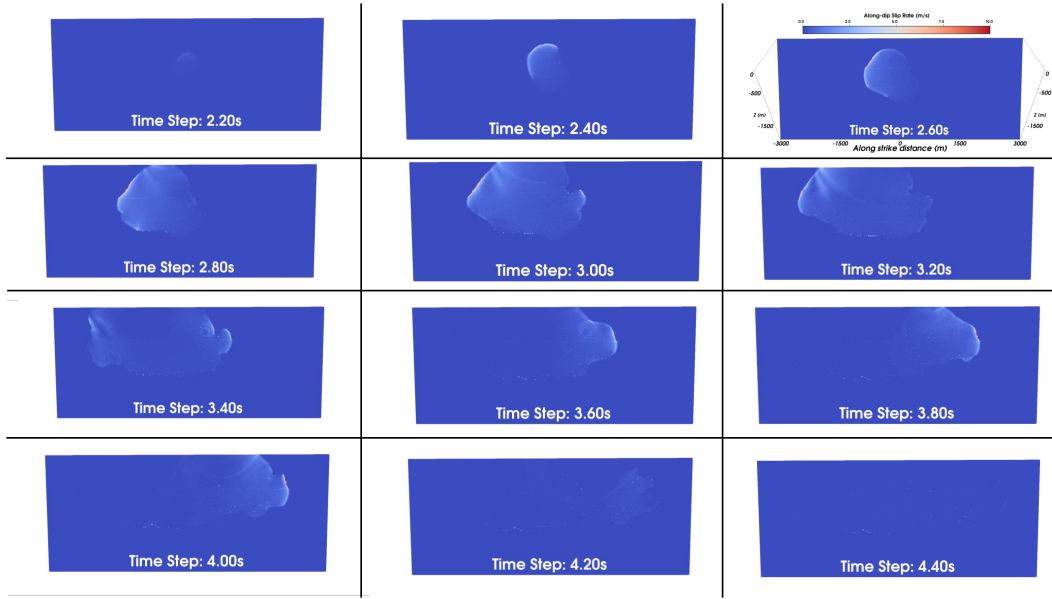


Figure 16: Along-dip slip rate evolution from 2.2 seconds to 4.4 seconds for the dynamic rupture model derived from strong-smoothed kinematic model

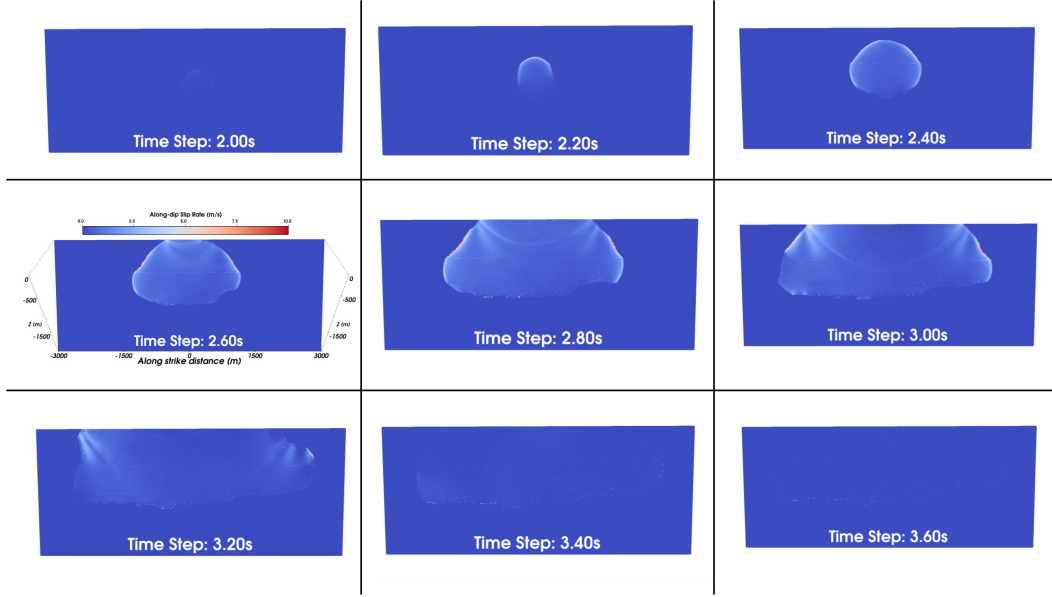


Figure 17: Along-dip slip rate evolution from 2.0 seconds to 3.6 seconds for the dynamic rupture model derived from low-smoothed kinematic model

3.4 Stress Drop

Figure 18 illustrates the along-dip shear stress drop after the rupture. The stress drop for both models generally falls within the same range. Notably, in both cases, the stress drop is positive in shallow layers (up to 300 m), with the largest stress drop occurring between depths of 500 m to 1000 m, ranging from 6 to 8 MPa. It's important to highlight that depths below 1 km are outside our scientific focus, as indicated by the negative S parameter. In other words, we initiated the seismic source at a depth of 1 km and then directed the rupture to propagate upward. The large value of the stress drop reflects that our S-parameter in the setup may be too small and simplistic.

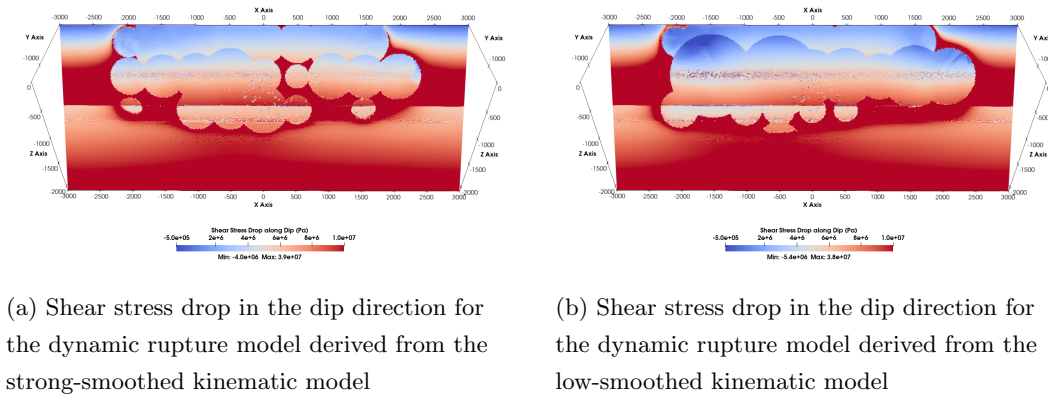
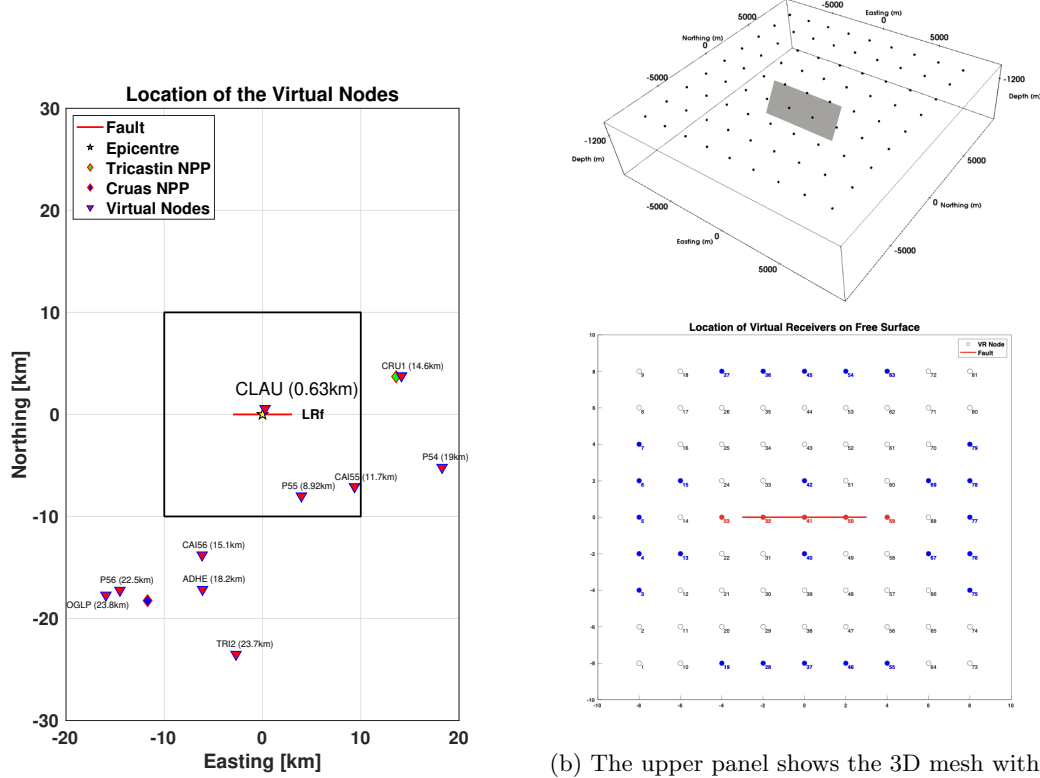


Figure 18: Comparison of along-dip stress drop between dynamic rupture models derived from strong- and low-smoothed kinematic models

4 Synthetic Ground Motion

We simulate synthetic ground motion (GM) at 81 equally spaced virtual receivers (VRs) placed on the surface. In Figure 19(a), the boundary of our mesh is outlined in a black box. Additionally, the figure shows the locations of several far-field observational stations and the Tricastin and Cruas nuclear power plants (NPPs).



(a) The map shows the locations of near-fault observational stations and two nuclear power plants (NPPs). The black box indicates the boundary of the computational mesh.

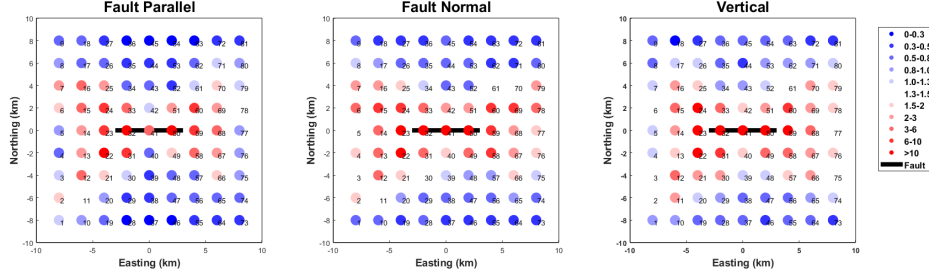
(b) The upper panel shows the 3D mesh with 81 virtual receivers (VRs) on the free surface. The lower panel shows the virtual nodes in a map view, with the red line indicating the location of the fault. Blue and red highlighted VRs are plotted below.

Figure 19

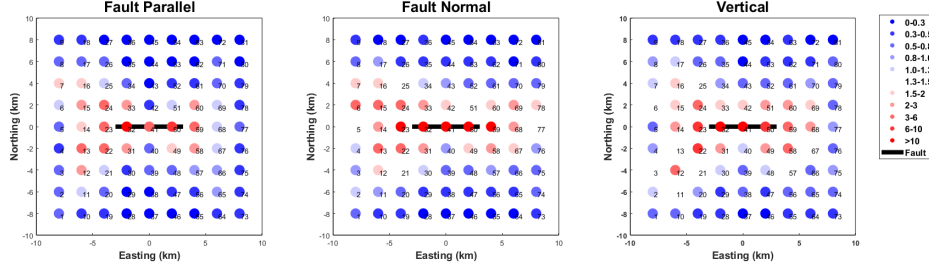
The PGA maps of both models are shown in Figure 20. These maps are comparable to the PGA map from Causse et al. (2021) Causse et al. (2021), which also illustrates an exceptional level of ground motion in the near-fault area.

The computed synthetic near-field GMs are plotted in acceleration. We compare dynamic rupture models derived from low- and strong-smoothed kinematic slip models, which exhibit distinctly different slip histories, to illustrate their impact on the computed GM.

Calibrating our synthetic near-fault ground motion (GM) is challenging due to the absence of recorded observational data within 10 km from the epicenter (LAURENDEAU et al., submitted), except for the station CLAU, which is positioned near the fault trace, approximately 600 meters from the epicenter. However, it offers limited usability in seismic frequency band and suffers from poor data quality (ref. Delouis, 2023).



(a) PGA map using low smoothed slip model



(b) PGA map using strong smoothed slip model

Figure 20

Based on our numerical simulation of the near-field ground motions (GMs), we draw the following conclusions from the two dynamic rupture models derived from the strong- and low-smoothed kinematic models:

- As depicted in Figure 21, on-fault receivers demonstrate ground motion amplitudes that locally exceed gravity, as observed in the horizontal and vertical components of VR23, VR32, VR41, VR50, and VR59.

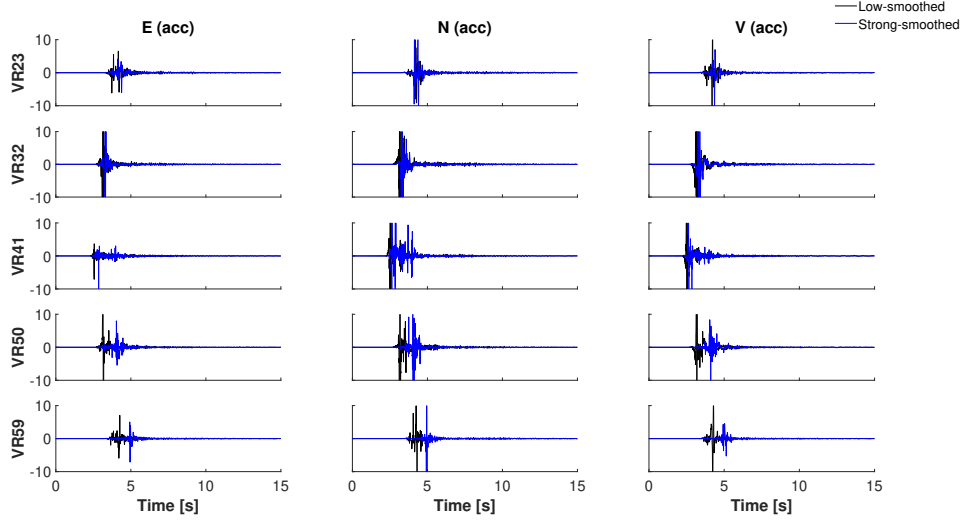


Figure 21: Near-fault synthetic accelerogram for near-fault virtual nodes (VR), excesses gravity

- As shown in Figure 22, strong directivity effects are evident, with significantly larger GM amplitudes observed in the direction of fault slip. For example, VR13 and VR15, located on the west side of the fault plane, and VR67 and VR69, located on the east side, experience ground motion amplitudes 2-3 times higher than those at stations perpendicular to the direction of rupture propagation, such as VR40 and VR42.

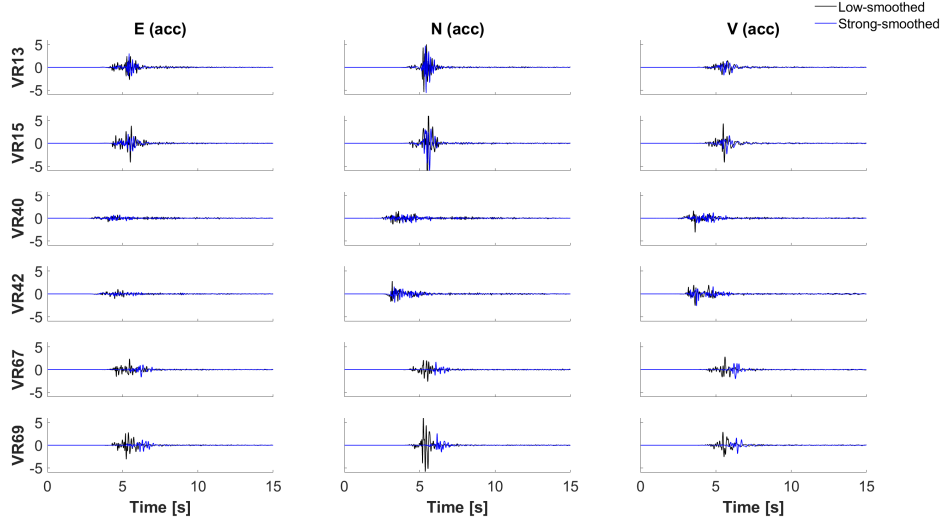


Figure 22: Near-fault synthetic accelerogram for near-fault virtual nodes (VR), strong directivity effect observed

- As shown in Figures 23 to 26, the difference becomes apparent when comparing fault-parallel and fault-normal VRs. The amplitude range for the former VRs is $[-1, 1] \text{ m/s}^2$, while for the latter, it is $[-2, 2] \text{ m/s}^2$. For the fault-normal VRs, the amplitude is similar in both directions. For the fault-parallel VRs, we expect the VRs situated on the hanging wall to have higher amplitudes due to reverse faulting. However, the simulation results still display similar amplitudes between the VRs on both hanging and footwalls. This could be due to the shallow hypocenter and suboptimal orientation of the dip angle for a reverse fault.

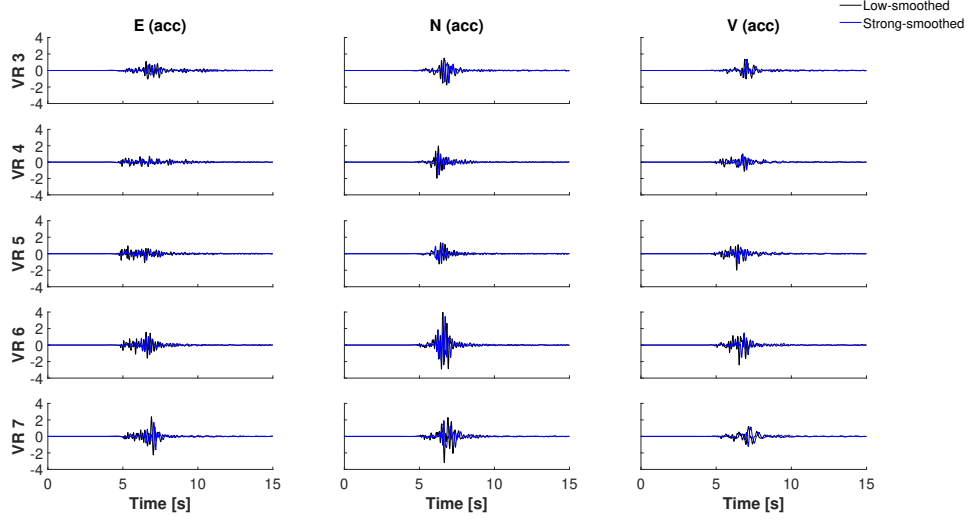


Figure 23: Synthetic accelerogram for fault-normal VRs in the west

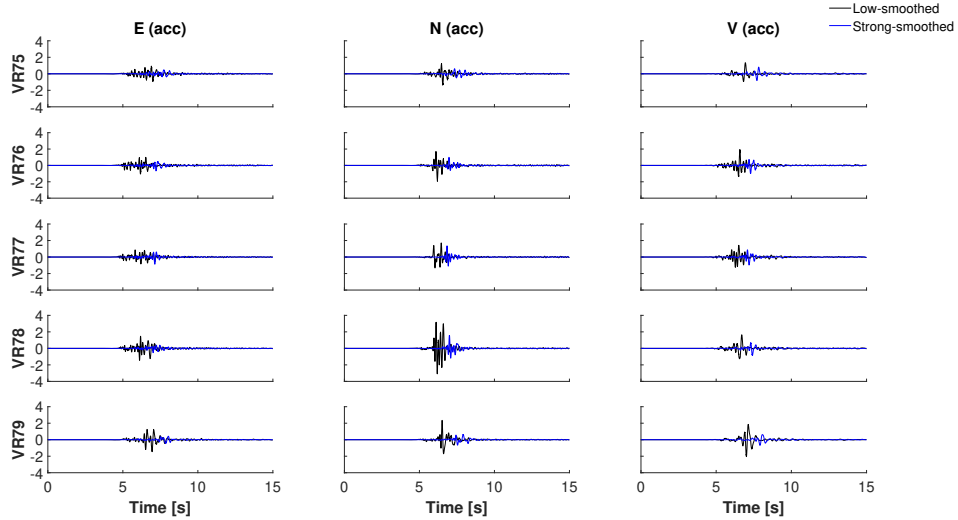


Figure 24: Synthetic accelerogram for fault-normal VRs in the east

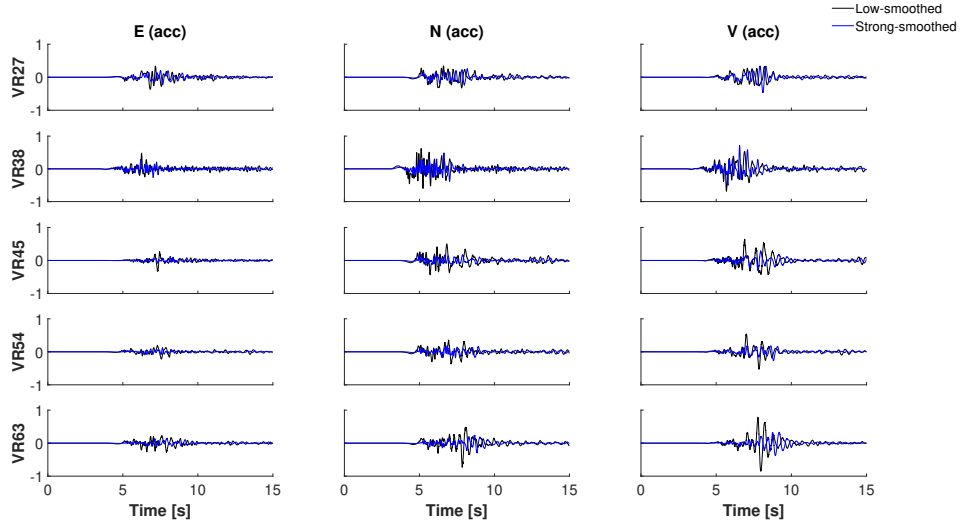


Figure 25: Synthetic accelerogram for fault-parallel VRs located on the foot wall (north)

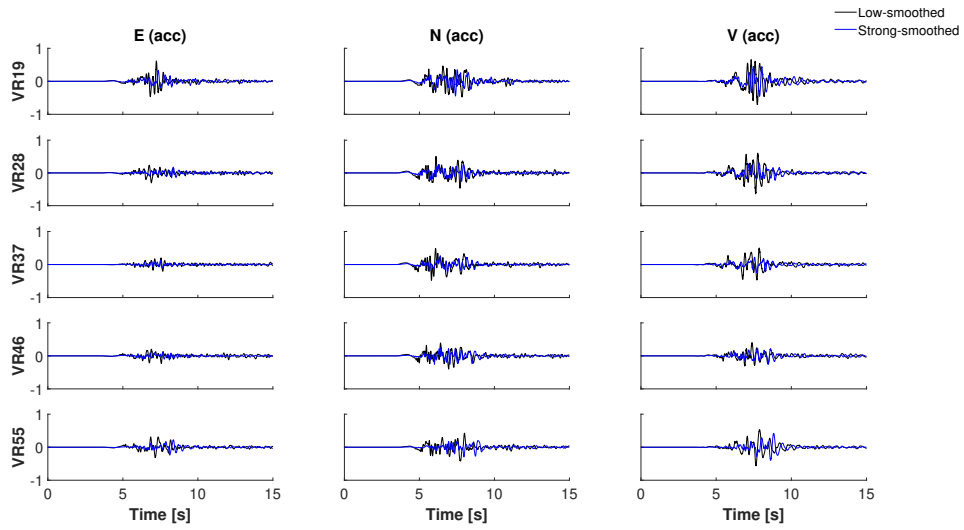
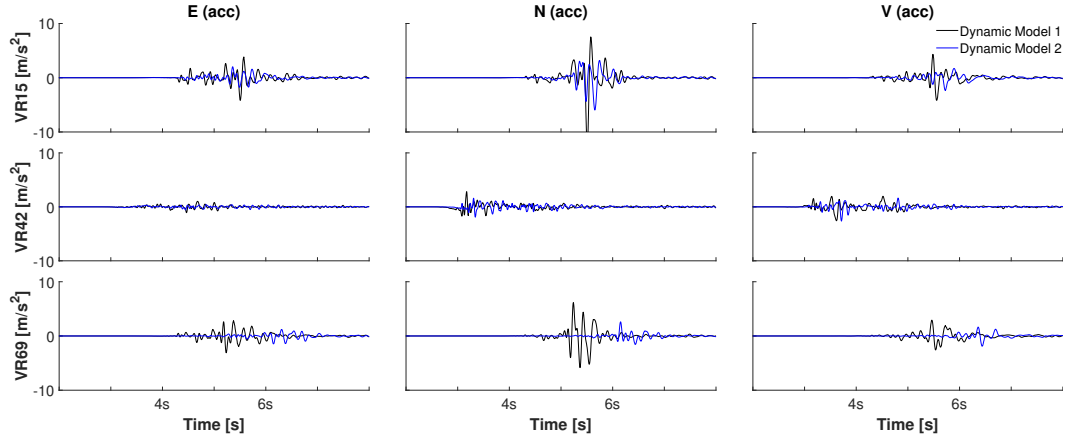


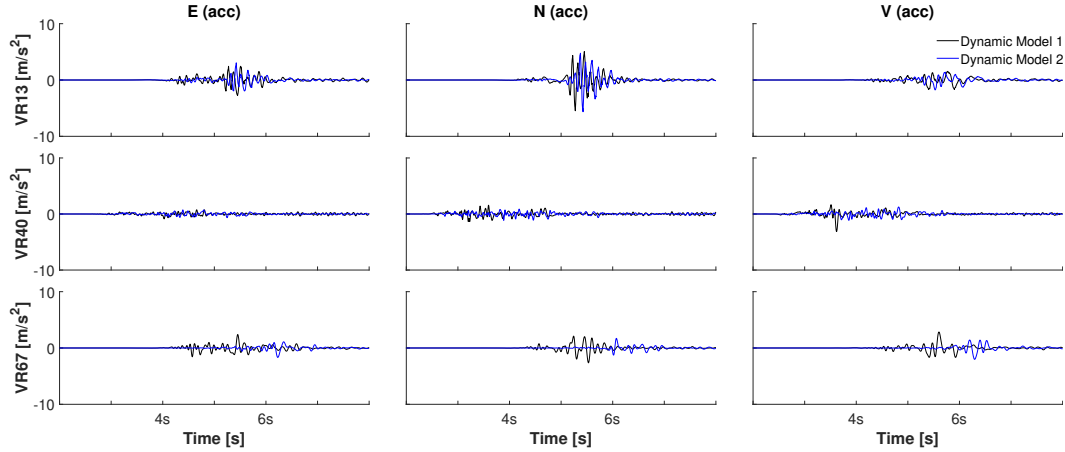
Figure 26: Synthetic accelerogram for fault-parallel VRs located on the hanging wall (south)

- In the low-smoothed model, simultaneous rupture occurs in all patches in both directions, resulting in higher ground motion (GM) amplitudes compared to the strong-smoothed model. In contrast, the strong-smoothed model exhibits sequential rupture propagation from left to right patches, releasing energy in stages. These differing rupture behaviors between the two models lead to variations in energy release rates and, consequently, GM amplitudes. For example, this phenomenon is very evident in VR78 and VR79.

Figure 27 shows the velocity waveforms of three receivers on both the footwall and hanging wall. Although we expect higher amplitudes on the hanging wall, this difference is not very apparent in the synthetic waveforms.”



(a) Velocity on foot wall



(b)

Figure 27: Velocity on hanging wall

5 Next Step: Simulate High-frequency Synthetics with 2D/3D Random Fractal Distribution of Heterogeneous Dynamic Parameters

We plan to simulate high-frequency components in near-fault ground motions following the method outlined by Ide et al. (2005). This involves incorporating dynamic rupture and fractal parameters, as fractal parameters introduce high-frequency components in the synthetics Gallovič & Valentová (2023) and Taufiqurrahman et al. (2022). Moreover, the impact of fault rupture with heterogeneous frictional parameters and fractal spatial distributions are discussed in studies by Venegas-Aravena et al. (2022) and Ide (2007).

Figure 28 shows a random fractal spatial distribution of dc on a planar fault plane. The dataset is generated by a MATLAB program created from a pseudo program published by Gallovič & Valentová (2023)

Previous studies have primarily focused on 2D fractal distributions on the fault plane. In this study, we could implement a 3D fractal distribution of spherical patches in *SeisSol*.

MATLAB code for creating a fractal spatial distribution of dc on a planar fault plane, following the algorithm provided by pseudocode describing the generation of a fractal template in Gallovič & Valentová (2023), D defines the fractal intensity, which determines the total number of fractals, increasing exponentially as this parameter rises. $Nlevels$ specifies the number of different sizes of fractals. L and W represent the fault length and width, respectively. nL and nW define the number of computing nodes along the fault length and width.

```
function delta = create_fractal(D, Nlevels, L, W, nL, nW)
    % Set parameters
    r0 = 1/8 * min(L, W);
    N0 = floor(L / W);
    dL = L / (nL - 1);
    dW = W / (nW - 1);
    patchCounter = 0;
    % Initialize template delta to all ones
    delta = ones(nL, nW);
    % Generate fractal patches
    for n = 0:Nlevels
        rn = r0 * 2^(-n);
        delta_n = 2^(-n);
        for nthLevelPatch = 1:(N0 * 2^(D * n))
            patchCounter = patchCounter + 1;
            centerStrike = rn + (L - 2 * rn) * rand();
            centerDip = rn + (W - 2 * rn) * rand();
            radius = rn;
            value = delta_n;
            % Determine the points inside the patch
            for j = 1:nW
                z = (j - 1) * dW;
                for i = 1:nL
                    x = (i - 1) * dL;
                    % Check if the point is inside the circular patch
                    if ((x - centerStrike)^2 + (z - centerDip)^2) <= radius^2
                        delta(i, j) = value;
                    end
                end
            end
        end
    end
end
```

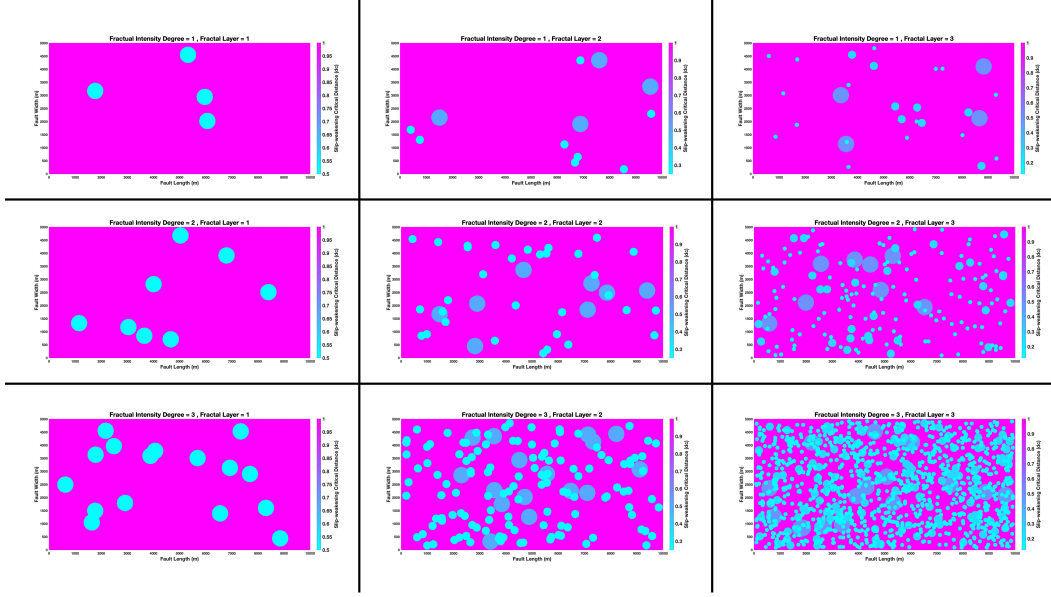
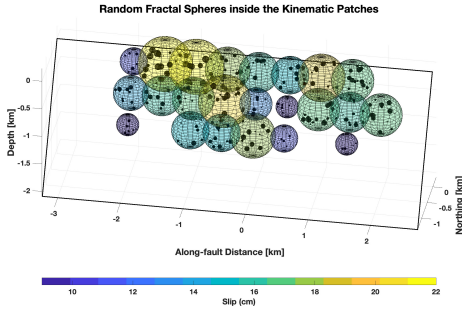
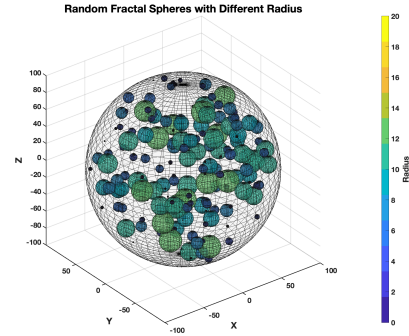


Figure 28: Fractal spatial distribution of dc on a planar fault plane. The figure displays increasing different sizes (layers) of fractals from left to right columns and increasing the total number of fractals from top to bottom rows.

467 end



(a) Demonstration of numerous smaller spheres randomly generated within each kinematic point source-related spherical patch. The quantity of spheres within each patch is correlated with the slip magnitude at each point source.



(b) Random spheres with varying radii are generated within an outer sphere. These radii serve as proxies for establishing heterogeneous critical slip-weakening distances (D_c).

6 Discussion and conclusions

We made several strong assumptions in the current model. The initial stress profile is configured with the S parameter set to negative below 1 km to prevent the rupture from propagating downwards and set to 0.2 above 1 km to facilitate spontaneous rupture. High cohesion was applied outside the spherical patches to stop the rupture and function as a boundary to define where the slip stops. Additionally, the critical slip-weakening distance D_c on the fault is correlated with the final slip. Furthermore, the velocity model used in the current model lacks details in the shallow depth, ignoring site effects.

Our model exhibits a high slip rate, exceeding 5 m/s at the rupture front (as referenced by Aochi et al. Aochi & Tsuda (2023), who reported 3 m/s). This disparity is likely attributed to differences in cohesion settings. We implemented a cohesionless condition within the patches, while Aochi et al. set cohesion to 5 MPa across the fault plane. Consequently, our model demonstrates a high rupture velocity of 2-3 km/s. In contrast, the kinematic model by Bertrand Delouis suggests an average rupture velocity of approximately 1 km/s, with some variations, particularly for ruptures in the northeast direction. For instance, the fastest speeds, up to 2.3 km/s, were observed when considering station CLAU in the inversion. Mordret et al. (2020) observed predominant lateral propagation towards the northeast and reported a rupture velocity of 2.8 km/s based on data from two closely spaced stations located approximately 90 km southeast of the earthquake epicenter.

Overall, we introduced a novel approach to linking the kinematic slip model to dynamic frictional parameters under the LSW friction law. We set the initial stress based on the assumed S -parameter and performed two dynamic rupture simulations using information derived from the kinematic model with different levels of smoothing. The simulation results show that fault slip has a strong impact on the resulting near-fault ground motions (NFGMs). Our analysis of the synthetic ground motions revealed a significant directivity effect, with near-fault receivers locally exceeding gravity under the current setup. Future work should focus on developing a more realistic initial stress profile based on strain continuity in layered crust, following Aochi and Tsuda. (2023). Additionally, we should use the updated dip angle (57 degrees) and experiment input parameters like μ_s , μ_d , and c to balance stress and friction parameters, ensuring the initial stress is not too large but sufficient to propagate across the predefined patch.

References

- Andrews, D. (1976). Rupture propagation with finite stress in antiplane strain. *Journal of Geophysical Research*, 81(20), 3575–3582.
- Aochi, H., & Tsuda, K. (2023). Dynamic rupture simulations based on depth-dependent stress accumulation. *Geophysical Journal International*, 233(1), 182–194.
- Bizzarri, A., & Cocco, M. (2003). Slip-weakening behavior during the propagation of dynamic ruptures obeying rate-and state-dependent friction laws. *Journal of Geophysical Research: Solid Earth*, 108(B8).
- Byerlee, J. (1978). Friction of rocks. *Rock friction and earthquake prediction*, 615–626.
- Causse, M., Cornou, C., Maufroy, E., Grasso, J.-R., Baillet, L., & El Haber, E. (2021). Exceptional ground motion during the shallow mw 4.9 2019 le teil earthquake, france. *Communications Earth & Environment*, 2(1), 14.
- Cornou, C., Ampuero, J.-P., Aubert, C., Audin, L., Baize, S., Billant, J., ... others (2021). Rapid response to the mw 4.9 earthquake of november 11, 2019 in le teil, lower rhône valley, france. *Comptes Rendus. Géoscience*, 353(S1), 1–23.
- Das, S., & Aki, K. (1977). A numerical study of two-dimensional spontaneous rupture propagation. *Geophysical journal international*, 50(3), 643–668.

- Delouis, B. (2014). Fmnear: Determination of focal mechanism and first estimate of rupture directivity using near-source records and a linear distribution of point sources. *Bulletin of the Seismological Society of America*, 104(3), 1479–1500.
- Delouis, B., Oral, E., Menager, M., Ampuero, J.-P., Trilla, A. G., Régnier, M., & Deschamps, A. (2021). Constraining the point source parameters of the 11 november 2019 mw 4.9 le teil earthquake using multiple relocation approaches, first motion and full waveform inversions. *Comptes Rendus. Géoscience*, 353(S1), 1–24.
- De Novellis, V., Convertito, V., Valkaniotis, S., Casu, F., Lanari, R., Monterroso Tobar, M. F., & Pino, N. A. (2020). Coincident locations of rupture nucleation during the 2019 le teil earthquake, france and maximum stress change from local cement quarrying. *Communications Earth & Environment*, 1(1), 20.
- De Novellis, V., Convertito, V., Valkaniotis, S., Casu, F., Lanari, R., Monterroso Tobar, M. F., & Pino, N. A. (2021). Author correction: Coincident locations of rupture nucleation during the 2019 le teil earthquake, france and maximum stress change from local cement quarrying. *Communications Earth & Environment*, 2(1), 47.
- Gabriel, A.-A., Ampuero, J.-P., Dalguer, L., & Mai, P. M. (2013). Source properties of dynamic rupture pulses with off-fault plasticity. *Journal of Geophysical Research: Solid Earth*, 118(8), 4117–4126.
- Gallovič, F., & Valentová, L. (2023). Broadband strong ground motion modeling using planar dynamic rupture with fractal parameters. *Journal of Geophysical Research: Solid Earth*, 128(6), e2023JB026506.
- Harris, R. A., Barall, M., Aagaard, B., Ma, S., Roten, D., Olsen, K., ... others (2018). A suite of exercises for verifying dynamic earthquake rupture codes. *Seismological Research Letters*, 89(3), 1146–1162.
- Ida, Y. (1972). Cohesive force across the tip of a longitudinal-shear crack and griffith's specific surface energy. *Journal of Geophysical Research*, 77(20), 3796–3805.
- Ide, S. (2007). Dynamic rupture propagation on a 2d fault with fractal frictional properties. *Earth, planets and space*, 59, 1099–1109.
- Masson, C., Mazzotti, S., Vernant, P., & Doerflinger, E. (2019). Extracting small deformation beyond individual station precision from dense global navigation satellite system (gnss) networks in france and western europe. *Solid Earth*, 10(6), 1905–1920.
- Mordret, A., Brenguier, F., Causse, M., Boué, P., Voisin, C., Dumont, I., ... Ampuero, J.-P. (2020). Seismic stereometry reveals preparatory behavior and source kinematics of intermediate-size earthquakes. *Geophysical research letters*, 47(17), e2020GL088563.
- Ohnaka, M. (2013). *The physics of rock failure and earthquakes*. Cambridge University Press.
- Palgunadi, K. H., Gabriel, A.-A., Ulrich, T., López-Comino, J. Á., & Mai, P. M. (2020). Dynamic fault interaction during a fluid-injection-induced earthquake: The 2017 m w 5.5 pohang event. *Bulletin of the Seismological Society of America*, 110(5), 2328–2349.
- Palmer, A. C., & Rice, J. R. (1973). The growth of slip surfaces in the progressive failure of over-consolidated clay. *Proceedings of the Royal Society of London. A. Mathematical and Physical Sciences*, 332(1591), 527–548.
- Ritz, J.-F., Baize, S., Ferry, M., Larroque, C., Audin, L., Delouis, B., & Mathot, E. (2020). Surface rupture and shallow fault reactivation during the 2019 mw 4.9 le teil earthquake, france. *Communications Earth & Environment*, 1(1), 10.
- Smerzini, V. M. P. R. e. a., C. (2022). Regional physics-based simulation of ground motion within the rhne valley, france, during the mw 4.9 2019 le teil earthquake. *Bull Earthquake Eng*, 21(1747–1774).
- Taufiqurrahman, T., Gabriel, A.-A., Ulrich, T., Valentova, L., & Gallovič, F. (2022).

- 573 Broadband dynamic rupture modeling with fractal fault roughness, frictional
 574 heterogeneity, viscoelasticity and topography: The 2016 mw 6.2 amatrice, italy
 575 earthquake. *Geophysical Research Letters*, 49(22), e2022GL098872.
- 576 Tinti, E., Casarotti, E., Ulrich, T., Taufiqurrahman, T., Li, D., & Gabriel, A.-A.
 577 (2021). Constraining families of dynamic models using geological, geodetic and
 578 strong ground motion data: The mw 6.5, october 30th, 2016, norcia earthquake,
 579 italy. *Earth and Planetary Science Letters*, 576, 117237.
- 580 Tinti, E., Cocco, M., Fukuyama, E., & Piatanesi, A. (2009). Dependence of slip
 581 weakening distance (d c) on final slip during dynamic rupture of earthquakes.
 582 *Geophysical Journal International*, 177(3), 1205–1220.
- 583 Ulrich, T., Gabriel, A.-A., Ampuero, J.-P., & Xu, W. (2019). Dynamic viability of
 584 the 2016 mw 7.8 kaikōura earthquake cascade on weak crustal faults. *Nature com-*
 585 *munications*, 10(1), 1213.
- 586 Ulrich, T., Vater, S., Madden, E. H., Behrens, J., van Dinther, Y., Van Zelst, I.,
 587 ... Gabriel, A.-A. (2019). Coupled, physics-based modeling reveals earthquake
 588 displacements are critical to the 2018 palu, sulawesi tsunami. *Pure and Applied*
 589 *Geophysics*, 176, 4069–4109.
- 590 Venegas-Aravena, P., Cordaro, E., & Laroze, D. (2022). Fractal clustering as spatial
 591 variability of magnetic anomalies measurements for impending earthquakes and
 592 the thermodynamic fractal dimension. *Fractal and Fractional*, 6(11), 624.
- 593 Zoback, M. L. (1992). First-and second-order patterns of stress in the lithosphere:
 594 The world stress map project. *Journal of Geophysical Research: Solid Earth*,
 595 97(B8), 11703–11728.